

Gravity Currents Produced by Lock Exchanges: Experiments and Simulations with a Two-Layer Shallow-Water Model with Entrainment

C. Adduce¹; G. Sciortino²; and S. Proietti³

Abstract: This paper presents the investigation of gravity currents by both laboratory experiments and a mathematical model. Eleven lock-exchange experiments, in which lock position, the initial current height, and density varied, were carried out to test the model validity and to compare laboratory results with previous expressions found in the literature. A two-layer shallow-water model was used to simulate all the runs. This model is new if compared with previous shallow-water models used to simulate gravity currents, because it accounts for both the entrainment and the free surface. A modified Turner's formula is used to model the entrainment between the two fluids. The developed shallow-water models with and without entrainment are also compared, showing a better agreement when mixing is accounted for. Also, the effect of the free surface is shown by comparing the developed two-layer shallow-water model with a free surface and two different single-layer models with a rigid-lid approximation. Laboratory experiments and model simulations, accounting for both the entrainment and the free surface, are in good agreement. Front velocities, measured during the slumping phase, were compared with both predicted ones and previous expressions found in the literature, showing in most of the cases better result when the developed model is used. DOI: 10.1061/(ASCE)HY.1943-7900.0000484. © 2012 American Society of Civil Engineers.

CE Database subject headings: Shallow water; Density currents; Entrainment; Experimentation; Mathematical models; Simulation.

Author keywords: Gravity currents; Shallow-water models; Density currents; Entrainment.

Introduction

Gravity currents develop when a heavier fluid flows under a lighter fluid, producing a zone of mixing between them. These phenomena are frequent in nature and in human activities. Examples of gravity currents are given by avalanches, turbidity currents, pyroclastic flows, lava flows, seabreezes, and salt wedge propagation (Simpson 1997).

Several numerical and experimental studies on gravity currents can be found in the literature. Von Kármán (1940) suggested a perfect-fluid model for deep gravity flows, propagating steadily. Prandtl (1952) presented a simplified theory on the beginning of the front motion, applicable just after the release of a heavier fluid into a lighter ambient fluid, whereas Benjamin (1968) derived a theory for the propagation of a steady two-dimensional (2D) gravity current in a rectangular channel. Hoult (1972) founded his analysis on shallow-water depth-averaged equations, supposing that the horizontal length scale of the current is much larger than the current thickness, and added a further condition, according to

which the Froude number just behind the head must be expressed by an experimental constant.

Huppert and Simpson (1980) proposed a numerical model assuming that the instantaneous current interface can be approximately simulated by rectangles that have the same area at each time step. Rottman and Simpson (1983) presented numerical solutions of the shallow-water equation for a two-layer fluid by applying an empirical front condition. More recently, Shin et al. (2004) developed, in agreement with their experimental results, an energy-conserving numerical model, in which the energy dissipation, for high Reynolds numbers, is a weak component. Marino et al. (2005) focused on the front condition, showing that the front Froude number is a function of the head Reynolds number. Some studies were focused on a more detailed description of gravity current dynamics by the implementation of high-resolution numerical models, such as LES (Hall and Meiburg 2004) or DNS (Härtel et al. 2000a, b; Cantero et al. 2006, 2007). These studies produce reliable results, but they are also extremely complex and require very high computational resources. Most of the preceding works described were developed using a particular experimental technique, called lock-exchange release.

This paper presents the investigation of lock-exchange gravity currents by both laboratory experiments and numerical simulations. Eleven lock-exchange experiments were performed. The lock position and initial height and density of the current were varied, and the space-time evolution of the gravity current was measured by an image analysis technique. A two-layer shallow-water model, accounting for both the free surface and the entrainment, was used to simulate all the runs. The effect of entrainment (i.e., the mass rate of clear water that crosses the interface between the two layers and mixes with the dense current) on the density current dynamics was tested, and the shallow-water models with and without entrainment are compared, showing a better agreement when mixing is

¹Assistant Professor, Dipartimento di Scienze dell'Ingegneria Civile, Università degli Studi Roma Tre, Via Vito Volterra 62, 00146 Rome, Italy (corresponding author). E-mail: adduce@uniroma3.it

²Associate Professor, Dipartimento di Scienze dell'Ingegneria Civile, Università degli Studi Roma Tre, Via Vito Volterra 62, 00146 Rome, Italy. E-mail: sciorti@uniroma3.it

³Ph.D. Student, Dipartimento di Scienze dell'Ingegneria Civile, Università degli Studi Roma Tre, Via Vito Volterra 62, 00146 Rome, Italy. E-mail: proietti@uniroma3.it

Note. This manuscript was submitted on July 29, 2008; approved on July 6, 2011; published online on July 8, 2011. Discussion period open until July 1, 2012; separate discussions must be submitted for individual papers. This paper is part of the *Journal of Hydraulic Engineering*, Vol. 138, No. 2, February 1, 2012. ©ASCE, ISSN 0733-9429/2012/2-111-121/\$25.00.

accounted for. In addition, the importance of free surface effect is shown by comparing the developed two-layer shallow-water model with a free surface and two different single-layer models with a rigid-lid approximation. A better agreement between measurements and predictions is obtained when the free surface is accounted for.

Experimental Apparatus and Laboratory Experiments

A series of 11 lock-exchange experiments were performed at the Hydraulics Laboratory of the University Roma Tre, Rome. All the experiments were run in a transparent Plexiglas tank (Fig. 1) of depth $h_0 = 0.3$ m, length $L = 3$ m, and width $b = 0.2$ m. The tank can be divided in two rectangular parts by a sliding gate, placed at a distance x_0 from the left wall of the tank, as shown in Fig. 1. The right part is filled with fresh water with a density $\rho_2 = 1,000$ kg/m³, and the left part is filled with salted and dyed water with a density $\rho_{01} > \rho_2$. At the beginning of each laboratory experiment, both the left and the right parts of the tank are filled to the same depth h_0 . The experiment starts when the sliding gate is suddenly removed, and a gravity current, flowing along the bottom of the tank and mixing with the ambient fluid, is generated.

A charged-coupled device (CCD) camera with a resolution of 712×576 pixels was used to record, with a frequency of 25 Hz, each laboratory experiment. All black and white images can be considered as matrices of gray levels, varying between 0 (black) to 255 (white). An image analysis technique is applied to measure the temporal evolution of the interface between the salty dyed water and clear water. First the images were cut to eliminate parts not useful for the detection of the gravity current interface. Then a threshold (i.e., gray level) corresponding to the mean value of gray levels in the gravity current had to be set to detect the instantaneous current interface, which is a discontinuity in the matrix of gray levels. This technique is useful to measure current interface with a high space-time resolution. The accuracy of the applied technique is 4 mm. All the measurements of the gravity current interface started 1 s after the gate removal, because the gravity current showed a very steep interface during its initial stage of development, and it was difficult to measure the current interfaces during this stage. Measurements of initial densities are performed by a pycnometer.

In each laboratory experiment, the gravity current can be classified as a Boussinesq's gravity current because the density ratio $\gamma = \rho_2/\rho_{01}$ is close to unity. The initial reduced gravity g'_0 of the dense fluid is defined as

$$g'_0 = g \frac{\rho_{01} - \rho_2}{\rho_{01}} \quad (1)$$

A mean Reynolds number R_m can be defined following Hacker et al. (1996) by

$$R_m = \frac{1}{2} \frac{V_{fm} h_0}{\nu} \quad (2)$$

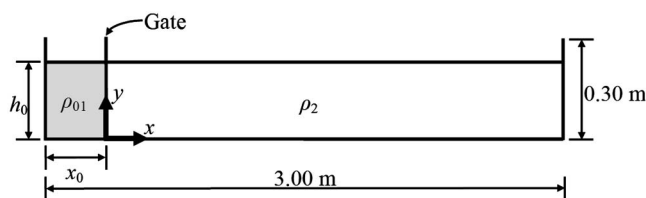


Fig. 1. Schematic view of the tank used to run laboratory experiments

Table 1. Experimental Parameters and mean Dimensionless Numbers

Run	x_0 (m)	h_0 (m)	ρ_{01} (kg/m ³)	γ (-)	g'_0 (m ² /s)	V_{fm} (m/s)	R_m (-)	F_H (-)
1	0.10	0.30	1,034	0.97	0.32	0.11	16,610	0.34
2	0.10	0.30	1,063	0.94	0.58	0.15	24,286	0.36
3	0.10	0.30	1,089	0.92	0.80	0.18	28,956	0.36
4	0.20	0.30	1,036	0.97	0.34	0.13	19,850	0.40
5	0.20	0.30	1,059	0.94	0.55	0.18	28,439	0.44
6	0.20	0.30	1,087	0.92	0.79	0.22	35,556	0.45
7	0.30	0.30	1,037	0.96	0.35	0.16	24,137	0.48
8	0.30	0.30	1,064	0.94	0.59	0.19	30,432	0.45
9	0.30	0.30	1,090	0.92	0.81	0.24	38,724	0.48
10	0.10	0.10	1,031	0.97	0.29	0.04	2,260	0.26
11	0.10	0.20	1,032	0.97	0.30	0.08	8,168	0.32

in which V_{fm} is the mean velocity of the gravity current front, measured during each run's duration, and ν is the kinematic viscosity. A total depth densimetric Froude number F_H is defined following Hacker et al. (1996) by

$$F_H = \frac{V_{fm}}{\sqrt{h_0 g'_0}} \quad (3)$$

A series of 11 laboratory experiments, shown in Table 1, was performed by varying three parameters: the distance between the left wall of the tank and the sliding gate (x_0); the initial depth of both salty and fresh water (h_0); and the initial density of salty water (ρ_{01}). The values of the mean front velocity (V_{fm}), the mean Reynolds numbers (R_m), and the total depth densimetric Froude numbers (F_H), for each run are also shown in Table 1.

Mathematical Model

Consider two homogeneous fluid layers of different density inside a prismatic and rectangular domain with a sloping bottom, in which θ is the angle between the bottom of the tank and the horizontal (Fig. 2). The dense fluid, with a density ρ_1 and a height $h_1(x, t)$, flows under the lighter fluid, with a constant density ρ_2 and a height $h_2(x, t)$, bounded at the top by a free surface. The heavier fluid flows with a speed V_1 , whereas the lighter one moves with a speed V_2 .

This paper presents the modeling of the free surface as a moving impermeable boundary, with a constant pressure distribution as a dynamical constraint. Previous papers (Rottman and Simpson 1983; Sparks et al. 1993; Klemp et al. 1994; Hogg et al. 1999;

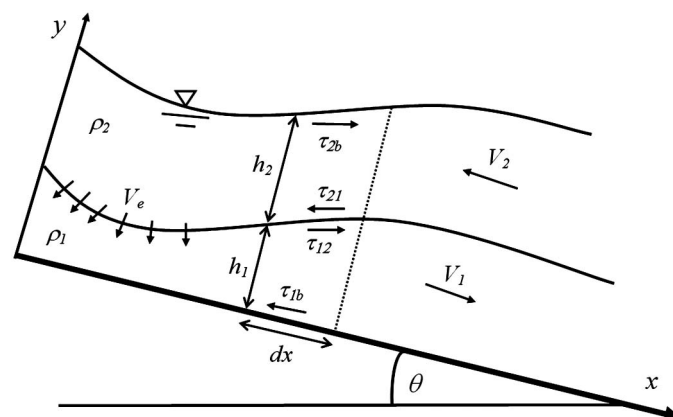


Fig. 2. Definition sketch for the mathematical model

Shin et al. 2004) used a similar numerical model (i.e., a shallow-water approximation) but with a rigid lid assumption, in which the preceding constraint is violated. These previous models, with a smaller number of equations, are simpler than the present model, but they are less similar to the physical phenomenon. In the present model, the interface between the dense and the lighter fluid is modeled as a moving permeable boundary, and then a certain fluid volume, estimated by an entrainment velocity V_e , flows from the upper layer to the lower layer. Because of the one-dimensionality of the fluid domain (the ratio of the tank's length and its depth is very large so that the flow is hydrostatic), the shallow-water hypothesis can be used. By applying the mass conservation and by projecting onto the x -axis, the momentum equation for each fluid domain of infinitesimal length dx (Fig. 2); after some manipulations, the following system of four differential equations is obtained:

$$\begin{aligned} \frac{\partial(\rho_1 h_1)}{\partial t} + \frac{\partial(\rho_1 h_1 V_1)}{\partial x} &= \rho_2 V_e \\ \frac{\partial(\rho_2 h_2)}{\partial t} + \frac{\partial(\rho_2 h_2 V_2)}{\partial x} &= -\rho_2 V_e \\ \frac{\partial(\rho_1 h_1 V_1)}{\partial t} + \frac{\partial}{\partial x} \left[\rho_1 h_1 V_1^2 + \left(\rho_2 h_2 + \rho_1 \frac{h_1}{2} \right) h_1 g \cos \theta \right] \\ &\quad - \rho_2 h_2 \frac{\partial h_1}{\partial x} g \cos \theta = \rho_1 g h_1 \sin \theta + V_1 \rho_2 V_e - \tau_{1b} - \tau_{21} \\ \frac{\partial(\rho_2 h_2 V_2)}{\partial t} + \frac{\partial}{\partial x} \left(\rho_2 h_2 V_2^2 + \rho_2 \frac{h_2^2}{2} g \cos \theta \right) + \rho_2 h_2 \frac{\partial h_1}{\partial x} g \cos \theta \\ &= \rho_2 g h_2 \sin \theta + V_2 (-\rho_2 V_e) + \tau_{2b} + \tau_{12} \end{aligned} \quad (4)$$

in which $V_e > 0$ is the entrainment velocity. The adopted signs for the shear stresses in the momentum equations make positive all the terms τ_{1b} , τ_{21} , τ_{2b} , and τ_{12} when $V_1 > 0$ and $V_2 < 0$ as it happens in lock-exchange simulations. Adopting the relation proposed by Supino (1981), the shear stresses at the interface are modeled by

$$\tau_{12} = \tau_{21} = \lambda_{\text{int}} \frac{\rho_1 + \rho_2}{2} \left[\frac{(V_1 - V_2)|V_1 - V_2|}{8} \right] \quad (5)$$

in which, following the experiments of Supino (1981), $\lambda_{\text{int}} = 0.316/\text{Re}_i^{0.25}$. The value τ_{1b} is the shear stress caused by the bottom and side walls for the lower layer, and τ_{2b} is the shear stress caused by the side walls for the upper layer. Both τ_{1b} and τ_{2b} are modeled by the Darcy-Weisbach friction formula, as in La Rocca et al. (2008):

$$\tau_{1b} = \lambda_1 \rho_1 \frac{V_1 |V_1|}{8} \left[\frac{(2h_1 + b)}{b} \right] \quad \tau_{2b} = -\lambda_2 \rho_2 \frac{V_2 |V_2|}{8} \frac{2h_2}{b} \quad (6)$$

The value λ_i , in which $i = 1$ for the lower layer and $i = 2$ for the upper layer, is given by the Colebrook's relation as

$$\lambda_i = \left\{ 2 \log \left[\frac{3.71}{(\varepsilon/h_i)} \right] \right\}^{-2} \left(1 + \frac{8h_i}{\text{Re}_i \varepsilon} \right) \quad (7)$$

In Eq. (7), ε is both the bottom and sidewalls' roughness, ε/h_i is the relative roughness of the i_{th} layer, and Re_i is a local Reynolds number, defined as

$$\text{Re}_i = \frac{V_i h_i}{\nu_i} \quad (8)$$

in which ν_i the kinematic viscosity of the i_{th} fluid layer.

The system of Eq. (4) cannot be written in conservation form using the components of the vector $\mathbf{U} \equiv (\rho_1 h_1, \rho_2 h_2, \rho_1 h_1 V_1, \rho_2 h_2 V_2)$ as conserved variables because of

the presence of the terms $\mp \rho_2 h_2 (\partial h_1 / \partial x) g \cos \theta$ in the momentum equations. As a result, Eq. (4) is not suitable to capture essential features of discontinuities. The terms $\mp \rho_2 h_2 (\partial h_1 / \partial x) g \cos \theta$ account for the projection along the x -direction of the normal stress at the interface because of the pressure field and vanish only when the local slope of the interface is the same as the bottom slope.

Starting from the system of Eq. (4), it is possible to derive an equivalent differential system but in conservation form, assuming as conserved variables the components of the vector $\mathbf{U} \equiv \{\rho_1 h_1, \rho_2 h_2, V_1, V_2\}$ and using the hypothesis that the density of the upper layer ρ_2 is constant ($\partial \rho_2 / \partial x = 0$, and $\rho_1(x, t)$ depends weakly on x , [i.e., $\rho_1 = \rho_1(t)$]. This hypothesis is a first approximation necessary to model the entrainment of density currents by a differential system in conservation form. In addition, the hypothesis that $\rho_1(x, t)$ depends weakly on x is justified by the measurements of the space-time variation of density in a lock-exchange gravity current shown in Nogueira (2011) and Nogueira (personal communication, 2011). By analyzing these density measurements it is possible to show how the neglected terms in the system Eq. (4), with the hypothesis $\rho_1 = \rho_1(t)$, are approximately 10% of the retained terms. A limit of the approximation $\rho_1 = \rho_1(t)$ is that at each time step, regions with a comparatively high entrainment rate are being diluted less than they should be, and regions of a comparatively low entrainment rate are being diluted more than they should be. In addition, with the hypothesis $\rho_1 = \rho_1(t)$ it is not possible to adequately model sustained pseudosteady flows, in which the spatial gradient of the dense layer plays an important role in the balance of the forces acting on the fluid, as in Ellison and Turner (1959).

After some calculations and taking into account the hypothesis described previously the system of differential Eqs. (4) assumes the conservation form

$$\begin{aligned} \frac{\partial(\rho_1 h_1)}{\partial t} + \frac{\partial(\rho_1 h_1 V_1)}{\partial x} &= \rho_2 V_e \\ \frac{\partial(\rho_2 h_2)}{\partial t} + \frac{\partial(\rho_2 h_2 V_2)}{\partial x} &= -\rho_2 V_e \\ \frac{\partial V_1}{\partial t} + \frac{\partial}{\partial x} \left[\frac{V_1^2}{2} + \left(\frac{\rho_2 h_2 + \rho_1 h_1}{\rho_1} \right) g \cos \theta \right] &= g \sin \theta - \frac{\tau_{1b} + \tau_{21}}{\rho_1 h_1} \\ \frac{\partial V_2}{\partial t} + \frac{\partial}{\partial x} \left[\frac{V_2^2}{2} + \left(\frac{\rho_1 h_1 + \rho_2 h_2}{\rho_2} \right) g \cos \theta \right] &= g \sin \theta + \frac{\tau_{2b} + \tau_{12}}{\rho_2 h_2} \end{aligned} \quad (9)$$

The explicit calculation of $\rho_1(t)$ is performed by

$$\rho_1(t) = \frac{M_1 + \int_0^t dt \int_0^{x_f(t)} \rho_2 V_e dx}{V_1 + \int_0^t dt \int_0^{x_f(t)} V_e dx} \quad (10)$$

in which $x_f(t)$ is the instantaneous position of the dense current front; M_1 and V_1 are the mass and volume, respectively, per unit span length at $t = 0$ of the lower layer; and the two integrals are the unit mass and unit volume entering into the lower layer through the interface in the time interval $(0, t)$.

To close the model, it is necessary to express the quantity V_e in terms of the variables V_1 , h_1 , ρ_1 , and ρ_2 . Ellison and Turner (1959) conducted a series of laboratory experiments with pseudosteady gravity currents propagating along a sloping bottom. On the basis of the Ellison and Turner (1959) experiments, Turner (1986) suggested the following formula for the entrainment of a gravity current:

$$\frac{V_e}{V_1} = \begin{cases} \frac{0.08F^2 - 0.1}{F^2 + 5} & F^2 \geq 1.25 \\ 0 & F^2 < 1.25 \end{cases} \quad (11)$$

in which V_e/V_1 = entrainment coefficient' and F = local densimetric Froude number of the heavier fluid, defined as

$$F = \frac{V_1}{\sqrt{h_1 \frac{\rho_1 - \rho_2}{\rho_1} g \cos \theta}} \quad (12)$$

The use of Eq. (11) into the system of equations in Eq. (9) does not result in a good agreement between numerical and laboratory results because this formula is not appropriate to predict the entrainment resulting from a gravity current produced by lock-exchange release experiments. For these experiments, squared densimetric Froude numbers F , evaluated by numerical simulations, rarely reached values higher than 1.25, and the use of Eq. (11) often did not allow the numerical entrainment's activation. In addition, as shown in the experiments by Cenedese et al. (2004) and Cenedese and Adduce (2008) and in the analysis by Cenedese and Adduce (2010), mixing in a density current occurs even for subcritical Froude numbers. Consequently, Turner's (1986) relation Eq. (11) was modified: the threshold on squared densimetric Froude numbers was removed; in the first relation of Eq. (11), the coefficient 0.08 was substituted by a calibration parameter of the model k ; and the term 0.1 was fixed as 0 to avoid a negative value of V_e/V_1 when $F^2 \leq 0.1/k$. The result of these changes in Turner's (1986) relation is a new formula with a calibration parameter k for the model, which was set to fit the measured current interfaces. The following formula for entrainment prediction is adopted for the model's simulations:

$$\frac{V_e}{V_1} = \frac{k \times F^2}{F^2 + 5} \quad (13)$$

in which k was assumed constant and was set by a comparison between measured and predicted gravity current interfaces. The value of k giving better results and used for all the numerical simulations was $k = 0.48$. This value of k gives, for the performed experiments and if a mean Froude number is used for calculations, a mean predicted entrainment coefficient $V_e/V_1 \cong 0.07$, which is in agreement with previous laboratory and field entrainment evaluations (Cenedese and Adduce 2008).

A bulk entrainment coefficient E_m for all the performed runs was estimated by applying a procedure similar to that described in Cenedese and Adduce (2008). By an analysis of the acquired experimental images the volume per unit width entrained by the gravity current during the whole duration of the experiment T_m was estimated. The entrained discharge per unit width is obtained by dividing the entrained volume per unit width by the time T_m . The ratio between the entrained discharge per unit width and the upper surface per unit width of the current gives an estimate of the laboratory entrainment velocity V_{em} ; then a bulk entrainment coefficient E_m can be evaluated as the ratio of the laboratory entrainment velocity and the mean velocity of the gravity current front V_{fm} (shown in Table 1). For runs 1–9, $1.6 \times 10^{-2} \leq E_m \leq 2 \times 10^{-2}$, whereas for run 10, $E_m \cong 2.5 \times 10^{-3}$, and for run 11, $E_m \cong 8 \times 10^{-3}$. For runs 1–9, the estimated bulk entrainment coefficient ($1.6 \times 10^{-2} \leq E_m \leq 2 \times 10^{-2}$) has the same order of magnitude of the entrainment relation [Eq. (13)] with $0.6 \leq F_m \leq 1.12$, whereas for run 10 ($E_m \cong 2.5 \times 10^{-3}$) and run 11 ($E_m \cong 8 \times 10^{-3}$), the entrainment relation [Eq. (13)] overestimates the measured one with $0.6 \leq F_m \leq 1.12$. Fig. 3 (adapted from Cenedese and Adduce 2008) shows a comparison of entrainment evaluations in the laboratory (Cenedese et al. 2004; Cenedese

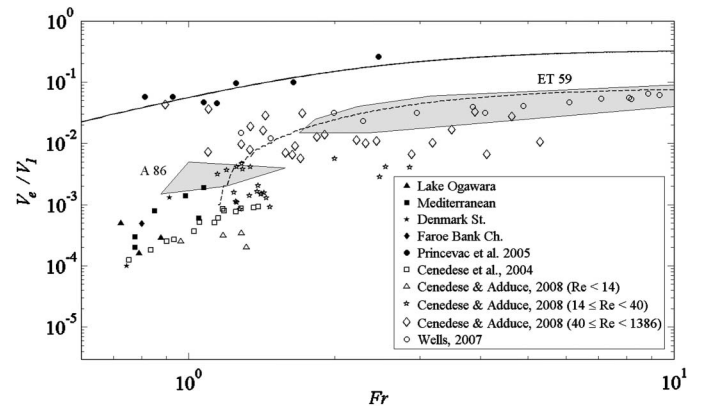


Fig. 3. Comparison of entrainment evaluations in the laboratory (open symbols) and in the field (solid symbols) with the entrainment formula [Eq. (13)] (black line) and the entrainment formula [Eq. (11)] suggested by Turner (1986) (dashed line) (data from Cenedese and Adduce 2008)

and Adduce 2008; Wells 2007; Ellison and Turner 1959; Alvia 1986) and observational studies (Price and Barringer 1994; Dallimore et al. 2001; Gorton and Sanford 2003; Mauritzen et al. 2005; Princevac et al. 2005) with the entrainment formula [Eq. (13)] and the entrainment formula [Eq. (11)] suggested by Turner (1986). For $F < 1.12$ (i.e., $F^2 < 1.25$), Eq. (11) predicts a 0 entrainment coefficient ($V_e/V_1 = 0$), and as a consequence, Eq. (11) cannot be used to simulate the performed experiments in which the mean F rarely reaches Turner's threshold value of $F = 1.12$. For $F > 1.12$ (i.e., $F^2 > 1.25$), Eq. (13) predicts entrainment values higher than Eq. (11); this behavior is supposed to be caused by the effect of R , as found in Cenedese and Adduce (2008) and Cenedese and Adduce (2010). Eq. (13) predicts larger entrainment than other laboratory experiments, with R up to 10^3 ; this behavior may be explained by a mixing transition that occurs for $R > 10^3$, as observed by the atmospheric measurements of Princevac et al. (2005). For runs 1–9, the mean Reynolds number R_m (Table 1) is high enough ($R_m \approx 10^4$) for a mixing transition to occur; this behavior is shown by the higher values of the measured entrainment ($1.6 \times 10^{-2} \leq E_m \leq 2 \times 10^{-2}$), if compared with other laboratory experiments with lower Reynolds numbers ($R \leq 10^3$). For runs 10 and 11, lower entrainment parameters were estimated ($E_m \cong 2.5 \times 10^{-3}$ and $E_m \cong 8 \times 10^{-3}$, respectively) compared with runs 1–9, because, owing to lower Reynolds numbers ($R_m \approx 10^3$), the mixing transition is not completely occurring.

The system of Eq. (4), with the hypothesis of fluid homogeneity (i.e., the density can change in time but not in space) can be expressed in the following conservation form:

$$\frac{\partial \mathbf{U}}{\partial t} + \frac{\partial \mathbf{F}(\mathbf{U})}{\partial x} = \mathbf{E}(\mathbf{U}) \quad (14)$$

in which $\mathbf{U} \equiv (\rho_1 h_1, \rho_2 h_2, V_1, V_2)$, $\mathbf{F}(\mathbf{U})$ and $\mathbf{E}(\mathbf{U})$ are vectors whose components are expressed in terms of \mathbf{U} , defined as

$$\mathbf{F}(\mathbf{U}) \equiv \left[\rho_1 V_1 h_1, \rho_2 V_2 h_2, \frac{V_1^2}{2} + \left(\frac{\rho_1 h_1 + \rho_2 h_2}{\rho_1} \right) g \cos \theta, \frac{V_2^2}{2} + \left(\frac{\rho_1 h_1}{\rho_1} + \frac{\rho_2 h_2}{\rho_2} \right) g \cos \theta \right] \quad (15)$$

$$\mathbf{E}(\mathbf{U}) \equiv \left[\rho_2 V_e, -\rho_2 V_e, g \sin \theta - \left(\frac{\tau_{1b} + \tau_{21}}{\rho_1 h_1} \right), g \sin \theta + \left(\frac{\tau_{2b} + \tau_{12}}{\rho_2 h_2} \right) \right] \quad (16)$$

The conservation form [Eq. (9)], if stress terms are neglected, imposes the conservation of energy across the front wave [for the case of a single layer, see Abbott (1979)] because $V_1^2/2$ and $V_2^2/2$ are the kinetic energy terms per unit mass. This assumption is quite realistic in many gravity currents phenomena (Benjamin 1968; Shin et al. 2004). The conservation form allows the application of numerical methods with good shock-capturing and shock-fitting features, which are important in problems concerned with the propagation of internal discontinuities. By expanding the derivatives in Eq. (9) and by using a matrix notation, the following system is obtained:

$$\frac{\partial \mathbf{U}}{\partial t} + \mathbf{A} \frac{\partial \mathbf{U}}{\partial x} = \mathbf{E}(\mathbf{U}) \quad (17)$$

in which \mathbf{A} = coefficients' matrix. An analysis on the eigenvalues of the matrix \mathbf{A} shows the presence of both complex and real eigenvalues, but the former are obtained only when the system's variables defined in \mathbf{U} assume extreme values, which were never reached in these experiments. The system can be classified as hyperbolic; this enables numerically solving the mathematical model [Eq. (9)] by a MacCormack's finite-difference scheme (Garcia and Kahawita 1986; Aureli et al. 2000, 2008), which is explicit, shock-capturing, and second-order accurate in space and time by a predictor-corrector method. The explicit formulation of this scheme is given by

$$\begin{aligned} \mathbf{U}_j^p &= \mathbf{U}_j^n - (dt/dx)[\mathbf{F}(\mathbf{U}_j^n) - \mathbf{F}(\mathbf{U}_{j-1}^n)] + dt\mathbf{E}(\mathbf{U}_j^n) & \text{predictor} \\ \mathbf{U}_j^c &= \mathbf{U}_j^p - (dt/dx)[\mathbf{F}(\mathbf{U}_{j+1}^p) - \mathbf{F}(\mathbf{U}_j^p)] + dt\mathbf{E}(\mathbf{U}_j^p) & \text{corrector} \\ \mathbf{U}_j^{n+1} &= \frac{\mathbf{U}_j^n + \mathbf{U}_j^c}{2} & \text{step } n+1 \end{aligned}$$

in which p and c denote predictor and corrector steps, respectively, $\mathbf{U}_j^n \equiv \mathbf{U}(jdx, ndt)$; and at each time step the sequence of

backward-forward difference for spatial derivatives is reversed. The adopted spatial mesh size is $dx = 0.015$ m, and the time step is given by the stability condition $dt \leq (dx/\Lambda)$, in which Λ is the maximum absolute value of the eigenvalues of the matrix \mathbf{A} .

Numerical Simulation of Gravity Current with and without Entrainment

The described mathematical model accounts for the entrainment between the dense and the lighter fluid by Eq. (13), in which the parameter k has to be tested. A first test was the simulation of a gravity current as an immiscible fluid (i.e., the parameter k was set to 0). Then different tests were performed with different values of k . The value of $k = 0.48$, which was used for all the simulations, assures a good fit between measurements and simulations.

If the mixing between the two fluids is not taken into account in the mathematical model (i.e., $k = 0$), the predicted immiscible current (dash-dotted line) is shallower than the predicted miscible current (solid line), as shown in Fig. 4. The expression [Eq. (13)] in the system [Eq. (9)] models the mass transfer between the two fluids; the effect of mixing is to produce a mass source in the first two equations of the system [Eq. (9)], which is a positive source in the first equation of the system [Eq. (9)] and a negative source (with the same value) in the second one. As a consequence, the depth of the heavier flow increases, if compared with the interface of an immiscible gravity current. The front speed of the immiscible current is higher than the front speed of the miscible current because in this latter model the entrainment (as the bed shear stress) affects directly the current interface and affects indirectly the front velocity. A similar behavior was shown in La Rocca et al. (2008), in which the authors observed some systematic discrepancies between the experimental and numerical results, owing to the absence of entrainment in the model.

Fig. 5 shows for run 1 a comparison between the experimental front advancing and numerical simulations with and without entrainment. Numerical simulations for immiscible fluids are able to reproduce the current dynamics until a certain time, after which the model cannot significantly represent the evolution of the front position. All the runs were simulated with and without entrainment,

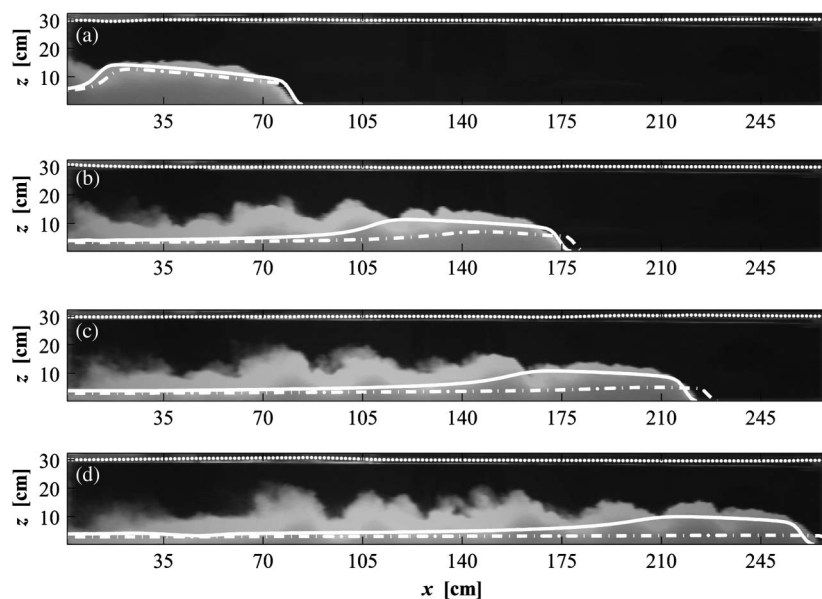


Fig. 4. Comparison of laboratory-measured and numerically predicted results: free surface (dotted line); current interface for miscible fluids with $k = 0.48$ (solid line); current interface for immiscible fluids with $k = 0$ (dash-dotted line); run 9 after release: (a) 3 s; (b) 7 s; (c) 9 s; (d) 11 s

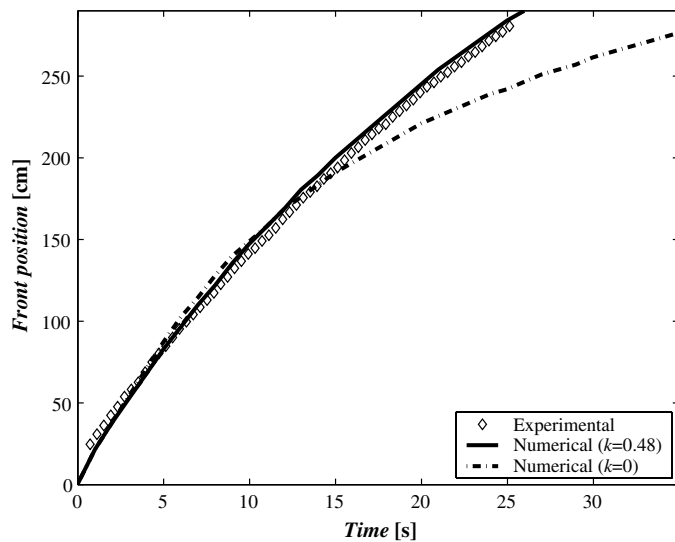


Fig. 5. Temporal evolution of front position for run 1: laboratory measurements (diamonds), numerical simulations for both miscible (solid line) and immiscible fluids (dash-dotted line)

and the results were always better when the entrainment was accounted for.

Numerical Comparison between a Two-Layer Model with Free Surface and Single-Layer Models with Rigid-Lid Approximation

Fig. 6 shows a comparison between laboratory measured and numerical predicted current interfaces by the proposed two-layer model with a free surface (solid line); a single-layer model with a rigid-lid approximation (SLM, dashed lines) with $\mathbf{U} \equiv (\rho_1 h_1, \rho_1 h_1 V_1)$ as variables and $\mathbf{F}(\mathbf{U}) \equiv [\rho_1 h_1 V_1, \rho_1 h_1 V_1^2 + (\rho_1 g' h_1^2/2)]$; and a single-layer model with a rigid-lid approximation (SLV, dotted lines) with $\mathbf{U} \equiv (\rho_1 h_1, V_1)$ as variables and $\mathbf{F}(\mathbf{U}) \equiv [\rho_1 h_1 V_1, (V_1^2/2 + g' h_1)]$. The single-layer models, whose results are shown in Fig. 6 by dotted and dashed lines, are obtained by the hypothesis $h_1 + h_2 = \text{constant}$ (i.e., a rigid-lid approximation) and by neglecting the equation of the upper layer. The

proposed two-layer model (solid line) shows good shock-fitting and shock-capturing properties, if compared with the shown single-layer models.

To explain the reason why the single-layer models do not bring to a good agreement between numerical simulations and experiments, it is useful to write the jump conditions across the front shock-wave for a system in conservation form (Duchateau and Zachmann 1986): $V_f \delta \mathbf{U} = \delta \mathbf{F}(\mathbf{U})$, in which V_f is the instantaneous front velocity, and the operator δ denotes the difference of the vectors across the shock. For the SLV model, it is easy to obtain $V_f = \sqrt{2g'h_f}$, whereas for the SLM model, $h_f = 0$, namely the shock cannot arise. The front conditions give a good explanation of the numerical simulations shown in Fig. 6; the velocity $V_f = \sqrt{2g'h_f}$ overestimates the front velocity if compared with other shock velocities, whereas the conditions $h_f = 0$ explains why the dashed interface has no shock front as shown in Fig. 6. For the two-layer model given by system [Eq. (14)], it is possible to obtain V_f by solving the jump conditions across the front shock-wave, but it needs a lot of calculations because of the solution of a cubic equation. When Boussinesq's condition is fulfilled (i.e., $\rho_2/\rho_1 \cong 1$, as in the performed experiments), V_f for two-layer model is very close to the front velocity predicted by Benjamin's equation (Benjamin 1968), in agreement with the good shock-fitting and shock-capturing properties of the developed model. On the contrary, the single-layer models are often used by imposing Benjamin's relation as a front velocity condition to have a good shock-capturing (Ungarish 2007; La Rocca et al. 2008). As a consequence, the single-layer models are able to simulate the shock-fitting, whereas the shock-capturing has to be imposed by a known front velocity. This limitation of single-layer models, according to the authors, is caused by the rigid-lid approximation, which needs to impose a fictitious longitudinal pressure gradient to avoid any free surface oscillations.

Comparison of Laboratory Measurements and Numerical Simulations

All the simulations were performed accounting for both the entrainment and the free surface. Fig. 7 shows the comparison for run 6 between laboratory measurements and numerical simulations with entrainment for both the interface between the two fluids (solid white

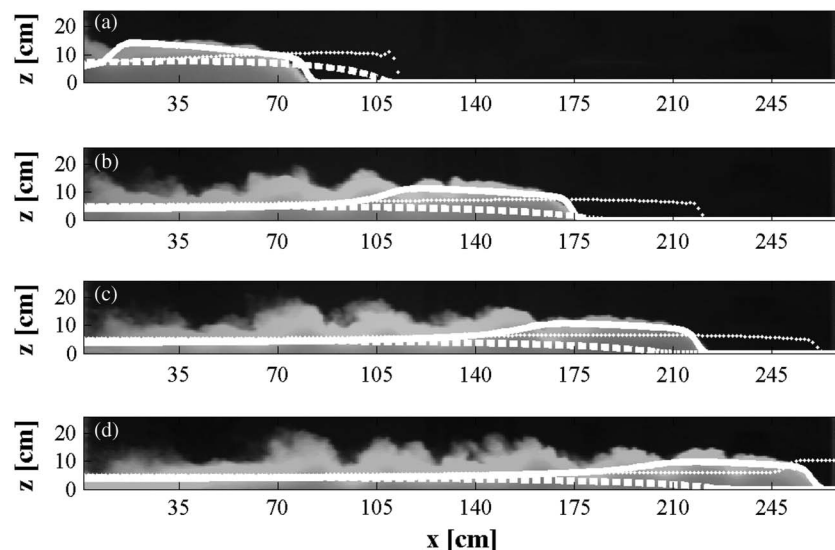


Fig. 6. Comparison of laboratory measured and numerical predicted currents interfaces; run 9 after release: (a) 3 s; (b) 7 s; (c) 9 s; (d) 11 s

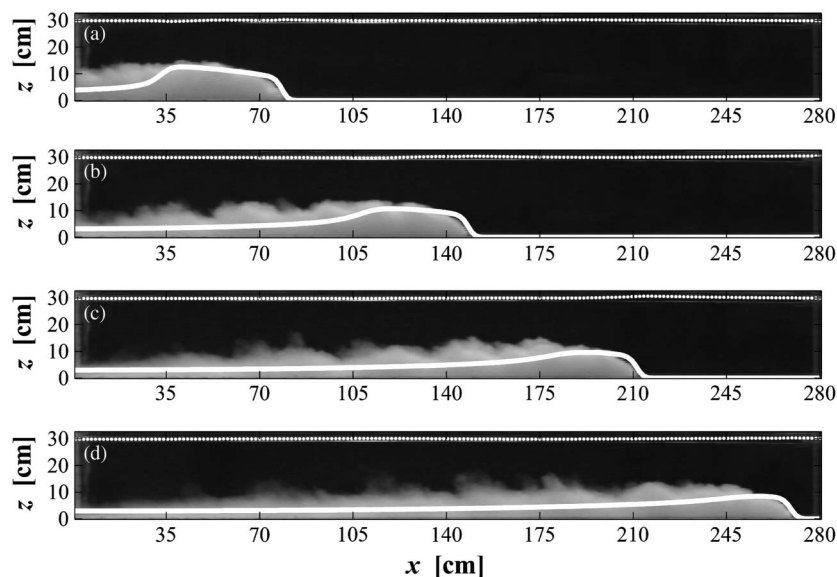


Fig. 7. Comparison of laboratory measured and numerical prediction with entrainment of gravity; run 6 after release (a) 3 s; (b) 6 s; (c) 9 s; (d) 12 s

lines) and the free surface (dotted white lines). After the gate removal, as shown in Fig. 7, the dense fluid collapses forming a gravity current flowing toward the right end wall, along the channel bottom. At the same time, the upper fluid forms a lighter gravity current propagating toward the left end wall. As the gravity current forms, it develops a characteristic head that is highly unstable and causes mixing between the dense gravity current and the ambient fluid. Two types of instabilities occur at the head of a gravity current: billows, which can be observed in Figs. 6 and 7, form in the region of velocity shear between the dense and the lighter fluid, and lobes and clefts (Simpson 1997) form by the influence of the bottom on the lower part of the leading edge of the dense current. This latter type of instability has a smaller scale if compared with billows and can be observed only with detailed photographs. The model tracks the current front both at the initial stage of the gravity current and when it is completely developed (Fig. 7). The mathematical model is not able to simulate the billows, which occur at the front rear (Fig. 7), or the lobes and clefts the use of shallow-water hypothesis, with depth-averaged quantities, prevents the model to represent such interfacial phenomena. Despite this limitation, the semiempirical entrainment model can take into account the mixing, owing to the instabilities at the interface, in the shallow-water framework.

Three distinct phases in the gravity current dynamics can be distinguished, focusing on the evolution of the front velocity (Simpson 1997; Marino et al. 2005). The first phase (slumping phase) is characterized by a time-constant front speed (i.e., a linearly varying front position), and it ends when the long wave of depression (produced by the reflection of the lighter flow on the left vertical wall), which is slightly faster than the current front, reaches this latter. Rottman and Simpson (1983) found that this behavior occurs when $x_f = l_{ss} \cong 10 \times x_0$ and that during the second phase (self-similar phase) the front speed U_f varies with $t^{-1/3}$ (i.e., the front position depends on time by a law $t^{2/3}$). When viscous effects become predominant, a third stage (viscous phase) can occur; in this case, the front velocity decreases with a law as $t^{-4/5}$ (and x_f increases with $t^{1/5}$); Huppert (1982) found that the transition between the self-similar phase and the viscous phase is reached when $x_f \cong l_{vis}$, in which l_{vis} is given by

$$l_{vis} = \left(\frac{g'_0 h_0^5 x_0^5}{\nu^2} \right)^{1/7} \quad (18)$$

Table 2 shows that laboratory experiments with $x_0 = 0.3$ m (runs 7–9) develop just the first phase because l_{ss} is equal to the tank's length ($l_{ss} = L = 3$ m). Runs 1–6 develop both the first and the second phase but do not develop the third one because l_{vis} is longer than the tank's length ($l_{vis} > L = 3$ m). The viscous phase develops only for runs 10 and 11, but the portion of the tank in which the third phase occurs is longer for run 10 ($L - l_{vis} = 1.20$ m) than for run 11 ($L - l_{vis} = 0.19$ m).

In Figs. 8–11 a comparison between the measured and simulated front positions is shown for all the performed laboratory experiments. Measurements of the front position were performed by a threshold method (i.e., the front position was found as the first position, starting from the right side of the figure; Fig. 7), in correspondence of which the height of the heavier fluid is higher than a fixed value. An increase of the initial density of the gravity current ρ_{01} produces a higher front speed, as shown in Figs. 8–10 and in Table 1. Figs. 8 and 9 show that both the measured and predicted front positions, after a first nearly linear variation, depend on time by a power-law. This behavior, in agreement with Rottman and Simpson (1983) and Simpson (1997), is caused by the development

Table 2. Starting Lengths of Self-Similar Phase and Viscous-Phase

Run	l_{ss} (m)	l_{vis} (m)
1	1.00	3.63
2	1.00	3.99
3	1.00	4.20
4	2.00	6.01
5	2.00	6.47
6	2.00	6.87
7	3.00	8.07
8	3.00	8.76
9	3.00	9.22
10	1.00	1.64
11	1.00	2.70

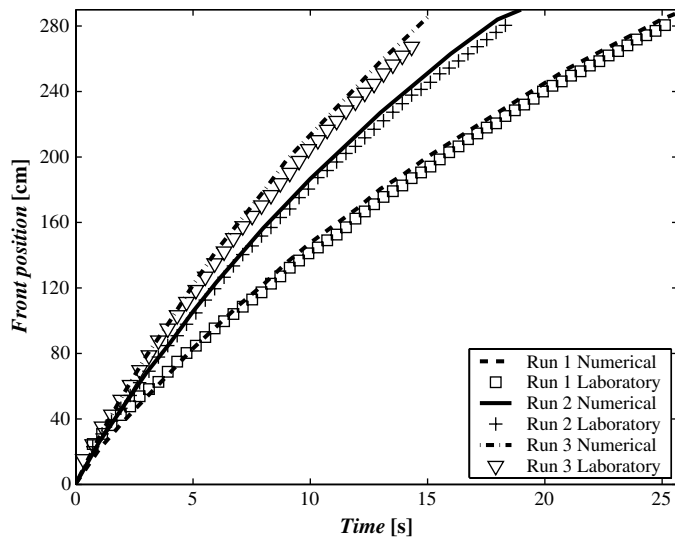


Fig. 8. Laboratory and numerical front position versus time

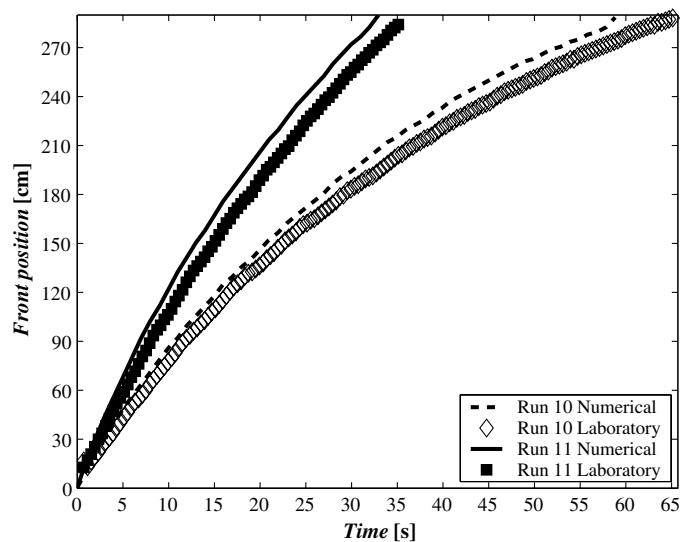


Fig. 11. Laboratory and numerical front position versus time

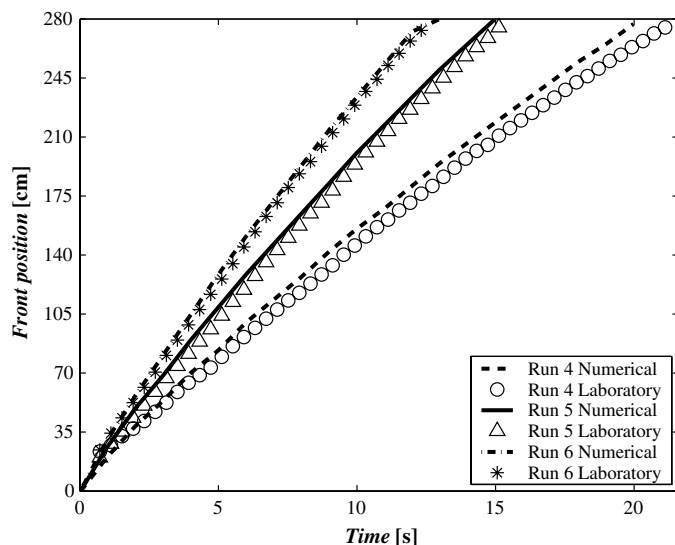


Fig. 9. Laboratory and numerical front position versus time

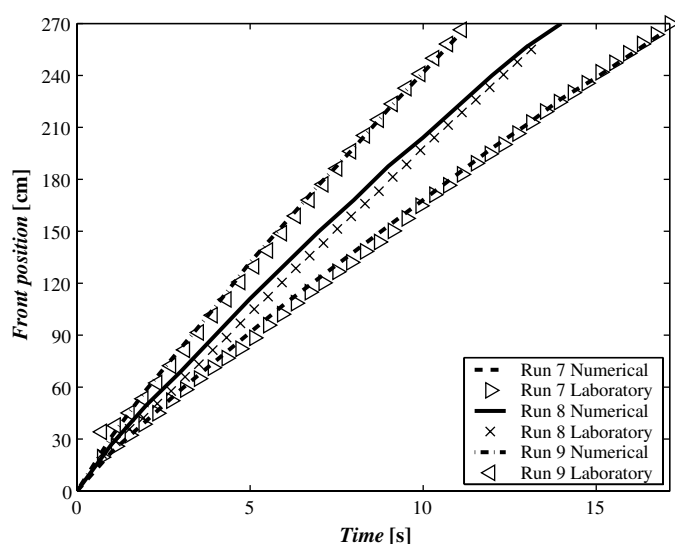


Fig. 10. Laboratory and numerical front position versus time

of both the slumping and self-similar phases for runs 1–6. Fig. 10 shows, in agreement with Rottman and Simpson (1983) and Simpson (1997), that both the measured and predicted front positions are linearly varying on time, because runs 7–9 develop only the slumping phase. Fig. 11 shows that, after a first nearly linear variation, both the measured and predicted front positions increase slower, if compared with the increase of the front positions shown in Figs. 8 and 9. This behavior is caused, in agreement with the literature, by the development of a third viscous phase in the gravity currents of runs 10 and 11. The average percentage between predictions and measurements of the front position for each run was evaluated. An agreement within 2–4% is observed for all the simulated front positions (Figs. 8–10), except for runs 10 and 11, in which the differences are approximately 6 and 9%, respectively (Fig. 11). The higher difference between measured and predicted front positions for runs 10 and 11 may be the result of the overestimation of the entrainment coefficient used in the simulations.

According to Marino et al. (2005), the dimensionless front position can be expressed as a function of the dimensionless time, as shown in Fig. 12 (laboratory experiments) and Fig. 13 (numerical

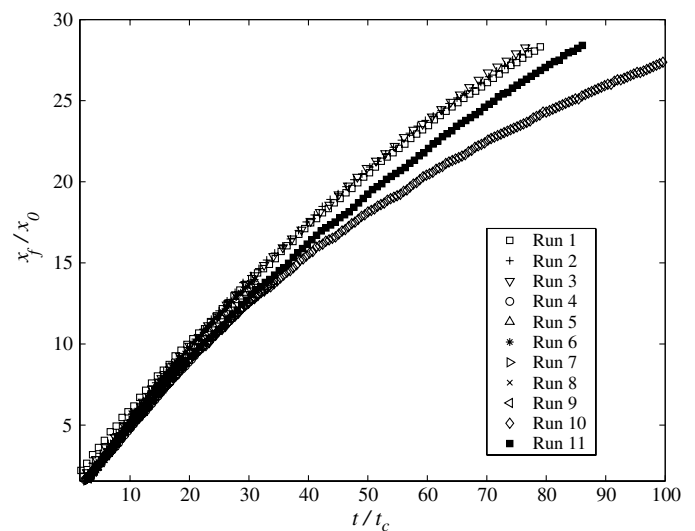


Fig. 12. Dimensionless laboratory front position versus dimensionless time for all runs

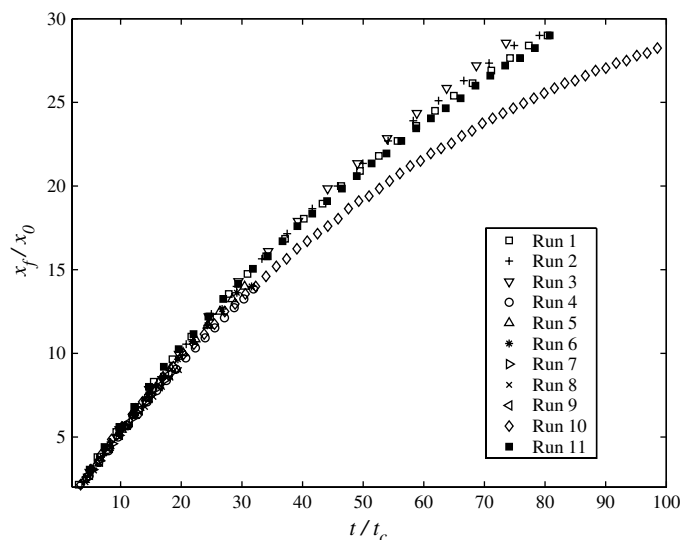


Fig. 13. Dimensionless numerical front position versus dimensionless time for all runs

simulations). Front positions x_f are scaled with the initial lock position x_0 , whereas the time scale t_c is defined by

$$t_c = \frac{x_0}{U_0} = \frac{x_0}{\sqrt{g'_0 h_0}} \quad (19)$$

in which $U_0 = \sqrt{g'_0 h_0}$ is a buoyancy velocity scale. Both laboratory (Fig. 12) and numerical (Fig. 13) dimensionless temporal evolution of the front positions are placed on the same curve, which is a straight line until the gravity currents develop just the slumping phase; then it becomes a power law when the self-similar phase occurs. The viscous phase develops only for runs 10 and 11, but the portion of the tank in which the third phase occurs is longer for run 10 ($L - l_{vis} = 1.20$ m) than for run 11 ($L - l_{vis} = 0.19$ m); then the dimensionless data for run 10, both in Figs. 12 and 13, are not collapsing on the dimensionless data of the other runs. Both the measured and predicted front positions were regressed by the previous defined laws; the estimated coefficient of determination R^2 are always higher than 0.997, showing a good agreement between present data and the literature.

Fig. 13 shows that the model is able to simulate all the phases of the gravity current evolution; the capacity of modeling the viscous phase is an unexpected feature of a shallow-water model. The resistance parameters of the shear stresses are modeled by Eq. (7), which allows to simulate a laminar friction law condition. A numerical test performed by Eq. (7) and the equation for high Reynolds numbers (i.e., $\lambda = \lambda_\infty$) showed a better agreement for the first case than for the second one. The use of Eq. (7), which is valid also when R is in the transition regimen, justifies the numerical agreement with laboratory results even in the so-called viscous phase.

The measured mean velocity of the gravity current during the first phase U_L , evaluated starting from the temporal evolution of the front advancing, was compared with both the velocity predicted by the present numerical model U_N and previous velocity relations found in the literature.

Benjamin (1968), analyzing a gravity current steadily propagating and energy conserving, proposed the following expression

$$\frac{U_{Ben}^2}{g' h_f} = \frac{(2h_0 - h_f)(h_0 - h_f)}{h_0(h_0 + h_f)} \quad (20)$$

in which h_f = front height.

Huppert and Simpson's (1980) formula

$$\frac{U_{HS}^2}{g' h_f} = \begin{cases} \frac{1}{4} \left(\frac{h_f}{h_0} \right)^{-\frac{2}{3}} & \frac{h_f}{h_0} \geq 0.075 \\ 1.4161 & \frac{h_f}{h_0} \geq 0.075 \end{cases} \quad (21)$$

is based on laboratory experiments with steady flows.

Rottman and Simpson's (1983) relation is given by

$$\frac{U_{RS}^2}{g' h_f} = \beta^2 \frac{(h_0 - h_f)(2h_0 - h_f)}{2h_0(h_0 + h_f)} \quad (22)$$

in which β = dimensionless constant (the authors suggested the value of 1), found for a shallow-water model and 2D two-layer flow based on a series of simplifying hypotheses.

Shin et al. (2004) proposed an expression that for the present laboratory experiments becomes

$$\frac{U_{SDL}^2}{g' h_f} = 1 - \frac{h_f}{h_0} \quad (23)$$

In all these formulas, there is the quantity h_f , the front height, whose experimental determination is uncertain; Huppert and Simpson (1980) used the height "just behind the head of the current," but this definition is rather ambiguous. Benjamin (1968) found that Eq. (21) reaches a maximum value when $h_f = 0.347 \times h_0$ (when a current reaches this height, the flow moves with the largest speed, and then the largest energy dissipation occurs); this value is used to obtain velocities in the previous equations.

Table 3 shows a comparison of the present laboratory U_L and numerical U_N front velocities and literature expressions given by Eqs. (20), (22), (23), and (23) for the slumping phase. All the predicted fronts velocities were made dimensionless by the measured front velocity U_L . In most cases, Benjamin's (1968) equation overestimates laboratory data because of the energy-conserving hypothesis, on which the formula in Eq. (21) is based; viscous dissipation tends to reduce the front velocity, so that Benjamin's (1968) formula rounds up the real velocity value). Instead, Rottman and Simpson's (1983) expression underestimates laboratory data because this formula was found by analyzing a two-layer flow bounded by horizontal rigid walls both at the top and at the bottom (the fluids have slightly different densities and must be inviscid, incompressible, and immiscible). All these constraints inevitably affect the speed's evaluation, resulting in values smaller than the real ones. This comparison of

Table 3. Laboratory Front Speed, Dimensionless Numerical Front Speed, and Dimensionless Expressions for Front Speed Prediction Found in the Literature

Run	U_L (m/s)	U_N/U_L (-)	U_{Ben}/U_L (-)	U_{HS}/U_L (-)	U_{RS}/U_L (-)	U_{SDL}/U_L (-)
1	0.14	1.14	1.21	0.93	0.86	1.00
2	0.21	1.00	1.10	0.86	0.76	0.90
3	0.24	1.04	1.13	0.88	0.79	0.96
4	0.14	1.07	1.21	1.00	0.86	1.07
5	0.19	1.05	1.16	0.89	0.84	1.00
6	0.23	1.04	1.17	0.91	0.83	0.96
7	0.16	1.00	1.06	0.88	0.75	0.94
8	0.19	1.00	1.21	0.95	0.84	1.00
9	0.24	1.00	1.13	0.92	0.79	0.96
10	0.07	1.14	1.29	1.00	1.00	1.14
11	0.11	1.18	1.18	1.00	0.82	1.00

laboratory and numerical data of the front velocity is encouraging; in several runs (particularly runs 7–9) laboratory and numerical values coincide, showing, as in the results of Shin et al. (2004), a better agreement if compared with previous formulas found in the literature.

Table 3 shows also that a change in lock position x_0 for gravity currents with the same initial density ρ_{01} and height h_0 does not affect current velocity, whereas both the initial density and initial height affect front velocity. The extension of a rectangular block is assumed as a first approximation to lock-exchange flow. If the decrease of potential energy is equated with the increase of kinetic energy, the following result is obtained: $U_0/(g'H)^{0.5} = 0.5$ (Simpson 1997). In the latter relation, U_0 is the front velocity, and H is the two-fluid layer depth; the only geometrical feature affecting the dynamics of gravity currents is the height. This simplified analysis fails when a gravity current reaches the self-similar phase, because the shape of the current changes, and the rectangular block hypothesis is no longer valid.

Conclusions

A laboratory and numerical analysis of 2D gravity current evolution was developed. Eleven lock-exchange experiments were carried out to test the model validity and to compare laboratory results with previous expressions found in the literature. A two-layer shallow-water model, accounting for both the entrainment of a density current and the free surface, is developed.

In previous papers using the shallow-water hypothesis, the free surface is modeled as a fixed impermeable boundary (i.e., a rigid-lid approximation is adopted). In this paper this constraint is removed, and the free surface is modeled as a moving boundary with a constant pressure. The interface between the two fluids is modeled as a moving permeable boundary, through which a quantity of mass, which is modeled by a modified Turner's (1986) formula, flows. The presented mathematical model is developed to reproduce lock-exchange experiments, in which the gravity currents are not pseudosteady, as in Ellison and Turner's (1959) experiments. Then Turner's (1986) expression was modified and replaced by a different law that allows modeling of the current dynamics. The capacity of modeling the mass transport between the two fluids constitutes an additional good feature of the presented work, because shallow-water models rarely present this peculiarity.

Although an adequate treatment of the variation of density as a result of the incorporation of fresh water near the front seems crucial in the simulation of lock-exchange currents, the adopted hypothesis $\rho_1 = \rho_1(t)$ (i.e., a homogeneous density of the lower layer at each time step), is a first approximation in the simulation of gravity currents with entrainment. In addition, the comparison between numerical simulations with both immiscible and miscible fluids shows that the former predicts with a better agreement the current height, the front shape, and the front position, even when the current reaches the viscous phase. Free surface effect was tested by comparing the developed two-layer shallow-water model, accounting for the free surface, and two different single-layer models with a rigid-lid approximation. In this latter simulation the developed two-layer shallow-water model showed better results.

All the experiments were simulated by the developed model showing a good agreement for both the current interfaces and front positions; the presented model is able to reproduce gravity current dynamics. Numerical and experimental front position shows three different stages in the gravity current dynamics: a first slumping phase, in which the front speed is time-constant; a second self-similar phase with a decelerating front velocity; and a third viscous phase, when viscous effects are prevalent.

The numerical and experimental velocities, evaluated during the first phase, are also compared with previous expressions found in the literature; in most of the runs numerical predictions show a better agreement if compared with previous formulas. This shows that the presented model is coherent with the problem, and is able to reproduce the front speed. In conclusion, the presented model can represent a valid tool for a technical-quantitative simulation of miscible gravity current evolution, thanks to a suitable compromise between representativeness and requested computational resources.

References

- Abbott, M. B. (1979). *Computational hydraulics, element of the theory of free surface flows*, Pitman, London, 31–34; 224–227.
- Alavian, V. (1986). "Behavior of density currents on an incline." *J. Hydraul. Eng.*, 112(1), 27–42.
- Aureli, F., Maranzoni, A., Mignosa, P., and Ziveri, C. (2008). "Dam break flows: Acquisition of experimental data through and imaging technique and 2D numerical modeling." *J. Hydraul. Eng.*, 134(8), 1089–1101.
- Aureli, F., Mignosa, P., and Tomirotti, M. (2000). "Numerical simulation and experimental verification of dam break flows with shocks." *J. Hydraul. Res.*, 38(3), 197–206.
- Benjamin, T. B. (1968). "Gravity currents and related phenomena." *J. Fluid Mech.*, 31(2), 209–248.
- Cantero, M., Balachandar, S., García, M., and Ferry, J. (2006). "Direct numerical simulations of planar and cylindrical density currents." *J. Appl. Mech.*, 73(6), 923–930, 10.1115/1.2173671.
- Cantero, M., Lee, J., Balachandar, S., and García, M. (2007). "On the front velocity of gravity currents." *J. Fluid Mech.*, 586, 1–39, 10.1017/S0022112007005769.
- Cenedese, C., and Adduce, C. (2008). "Mixing in a density-driven current flowing down a slope in a rotating fluid." *J. Fluid Mech.*, 604, 369–388.
- Cenedese, C., and Adduce, C. (2010). "A new entrainment parameterization for mixing in overflows." *J. Phys. Oceanogr.*, 40(8), 1835–1850.
- Cenedese, C., Whitehead, J. A., Ascarelli, T. A., and Ohiwa, M. (2004). "A dense current flowing down a sloping bottom in a rotating fluid." *J. Phys. Oceanogr.*, 34(1), 188–203.
- Dallimore, C. J., Imberger, J., and Ishikawa, T. (2001). "Entrainment and turbulence in saline underflow in Lake Ogawara." *J. Hydraul. Eng.*, 127(11), 937–948.
- Duchateau, P., and Zachmann, D. W. (1986). "Partial differential equations." *Schaums outlines series in mathematics*, McGraw-Hill, New York.
- Ellison, T. H., and Turner, J. S. (1959). "Turbulent entrainment for stratified fluids." *J. Fluid Mech.*, 6(3), 423–448.
- Garcia, R., and Kahawita, R. A. (1986). "Numerical solutions of the De Saint Venant equations with the Mac-Cormack finite difference scheme." *Int. J. Numer. Methods Fluids*, 6(5), 259–274.
- Girton, J. B., and Sanford, T. B. (2003). "Descent and modification of the overflow plume in Denmark Strait." *J. Phys. Oceanogr.*, 33(7), 1351–1364.
- Hacker, J., Linden, P. F., and Dalziel, S. B. (1996). "Mixing in lock release gravity currents." *Dyn. Atmos. Oceans*, 24(1–4), 183–195.
- Hall, B., and Meiburg, E. (2004). *Large eddy simulation on particle driven gravity currents*, International Mathematics Meeting Center (CIRM), Marseille, France.
- Härtel, C., Meiburg, E., and Necker, F. (2000a). "Analysis and direct numerical simulation of the flow at a gravity current head. Part 1: Flow topology and front speed for slip and no-slip boundaries." *J. Fluid Mech.*, 418, 189–212.
- Härtel, C., Carlsson, F., and Thunblom, N. (2000b). "Analysis and direct numerical simulation of the flow at a gravity current head. Part 2: The lob-and-cleft instability." *J. Fluid Mech.*, 418, 213–229.
- Hogg, A. J., Huppert, H. E., and Hallworth, M. A. (1999). "Reversing buoyancy of particle-driven gravity currents." *Phys. Fluids*, 11(10), 2891–2900.

- Hoult, D. P. (1972). "Oil spreading on the sea." *Ann. Rev. Fluid Mech.*, 4(1), 341–368.
- Huppert, H. E. (1982). "The propagation of two-dimensional and axisymmetric viscous gravity currents over a rigid horizontal surface." *J. Fluid Mech.*, 121(1), 43–58.
- Huppert, H. E., and Simpson, J. E. (1980). "The slumping of gravity currents." *J. Fluid Mech.*, 99(4), 785–799.
- Klemp, Rotunno, and Skamarock (1994). "On the dynamics of a gravity current in a channel." *J. Fluid Mech.*, 269, 169–198.
- La Rocca, M., Adduce, C., Sciortino, G., and Bateman, P. A. (2008). "Experimental and numerical simulation of three-dimensional gravity currents on smooth and rough bottom." *Phys. Fluids*, 20(10), 106603.
- Marino, B. M., Thomas, L. P., and Linden, P. F. (2005). "The front condition of gravity currents." *J. Fluid Mech.*, 536, 49–78.
- Mauritzen, C., Price, J., Sanford, T., and Torres, D. (2005). "Circulation and mixing in the faroese channels." *Deep-Sea Res., Part II*, 52(6), 883–913.
- Nogueira, H. I. S. (2011). "Time and space analysis of entrainment on density currents." *Proc., Int. Conf. XXXIV IAHR*, Engineers Australia, Brisbane, Australia.
- Prandtl, L. (1952). *Essentials of fluid dynamics*, Blackie & Son, London.
- Price, J. F., and Barringer, M. O. (1994). "Outflows and deep water production by marginal seas." *Prog. in Oceanogr.*, 33(3), 161–200.
- Princevac, M., Fernando, H. J. S., and Whiteman, D. C. (2005). "Turbulent entrainment into natural gravity driven flows." *J. Fluid Mech.*, 533, 259–268.
- Rottman, J. W., and Simpson, J. E. (1983). "Gravity currents produced by instantaneous releases of a heavy fluid in a rectangular channel." *J. Fluid Mech.*, 135, 95–110.
- Shin, J. O., Dalziel, S. B., and Linden, P. F. (2004). "Gravity currents produced by lock-exchange." *J. Fluid Mech.*, 521, 1–34.
- Simpson, J. E. (1997). *Gravity currents in the environment and the laboratory*, 2nd Ed., Cambridge University Press.
- Sparks, R. S., et al. (1993). "Sediment-laden gravity currents with reversing buoyancy." *Earth Planet. Sci. Lett.*, 114(2–3), 243–257.
- Supino, G. (1981). *Manuale dell'ingegneria civile*, Edizioni Scientifiche A. Cremonese, Rome, 242–246.
- Turner, J. S. (1986). "Turbulent entrainment: The development of the entrainment assumption, and its application to geophysical flows." *J. Fluid Mech.*, 173, 431–471.
- Ungarish, M. (2007). "A shallow-water theory for high-Reynolds-number gravity currents for a wide range of density differences and fractional depths." *J. Fluid Mech.*, 579, 373–382.
- Von Kármán, T. (1940). "The engineer grapples with nonlinear problems." *Bull. Am. Math. Soc.*, 46(8), 615–683.
- Wells, M. G. (2007). "Influence of Coriolis forces on turbidity currents and their sediment patterns." *Particle-laden flow*, Springer, Netherlands.